Ahmed, Faisal; Rodríguez-Fernández, Carlos; Fernandez, Henry A.; Zhang, Yi; Shafi, Abde Mayeen; Uddin, Md Gius; Cui, Xiaoqi; Yoon, Hoon Hahn; Mehmood, Naveed; Liapis, Andreas C.; Yao, Lide; Caglayan, Humeyra; Sun, Zhipei; Lipsanen, Harri

Deterministic Polymorphic Engineering of $MoTe_2$ for Photonic and Optoelectronic Applications

Published in:
Advanced Functional Materials

DOI:
10.1002/adfm.202302051

Published: 15/08/2023

Document Version
Publisher's PDF, also known as Version of record

Nanoelectronics and Its New Materials – A NEW ERA OF NANOSCIENCE

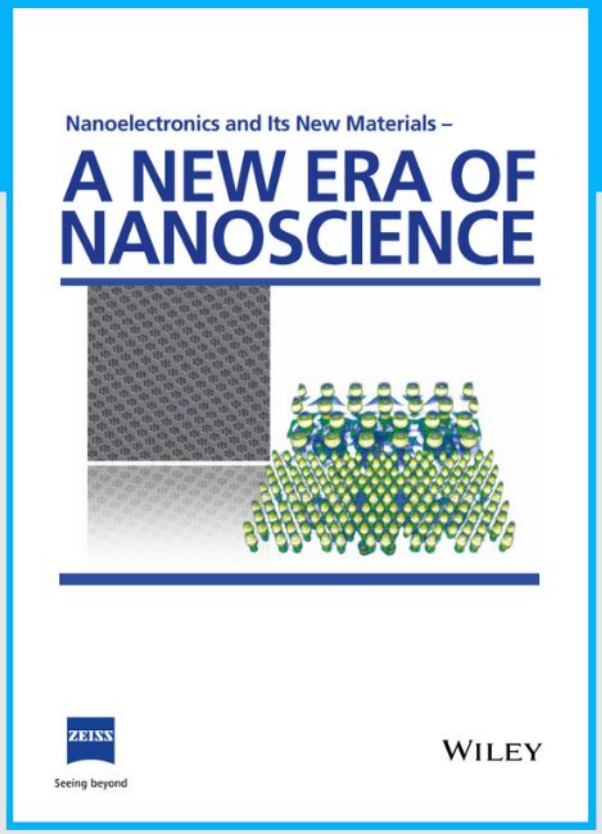

Discover the recent advances in electronics research and fundamental nanoscience.

Nanotechnology has become the driving force behind breakthroughs in engineering, materials science, physics, chemistry, and biological sciences. In this compendium, we delve into a wide range of novel applications that highlight recent advances in electronics research and fundamental nanoscience. From surface analysis and defect detection to tailored optical functionality and transparent nanowire electrodes, this eBook covers key topics that will revolutionize the future of electronics.

To get your hands on this valuable resource and unleash the power of nanotechnology, simply download the eBook now. Stay ahead of the curve and embrace the future of electronics with nanoscience as your guide.

ZEISS

Seeing beyond

WILEY

ADVANCED FUNCTIONAL MATERIALS
www.afm-journal.de

Deterministic Polymorphic Engineering of $MoTe_2$ for Photonic and Optoelectronic Applications

Faisal Ahmed, Carlos Rodríguez-Fernández, Henry A. Fernandez, Yi Zhang, Abde Mayeen Shafi, Md Gius Uddin, Xiaoqi Cui, Hoon Hahn Yoon, Naveed Mehmood, Andreas C. Liapis, Lide Yao, Humeyra Caglayan, Zhipei Sun, and Harri Lipsanen**

Developing selective and coherent polymorphic crystals at the nanoscale offers a novel strategy for designing integrated architectures for photonic and optoelectronic applications such as metasurfaces, optical gratings, photodetectors, and image sensors. Here, a direct optical writing approach is demonstrated to deterministically create polymorphic 2D materials by locally inducing metallic 1T′-$MoTe_2$ on the semiconducting 2H-$MoTe_2$ host layer. In the polymorphic-engineered $MoTe_2$, 2H- and 1T′- crystalline phases exhibit strong optical contrast from near-infrared to telecom-band ranges (1–1.5 μm), due to the change in the band structure and increase in surface roughness. Sevenfold enhancement of third harmonic generation intensity is realized with conversion efficiency (susceptibility) of ≈1.7×10^{-7} (1.1×10^{-19} m^2 V^{-2}) and ≈1.7×10^{-8} (0.3×10^{-19} m^2 V^{-2}) for 1T′ and 2H-$MoTe_2$, respectively at telecom-band ultrafast pump laser. Lastly, based on polymorphic engineering on $MoTe_2$, a Schottky photodiode with a high photoresponsivity of 90 AW^{-1} is demonstrated. This study proposes facile polymorphic engineered structures that will greatly benefit realizing integrated photonics and optoelectronic circuits.

1. Introduction

Polymorphism is the coexistence of different crystalline structures with the same chemical composition in a single material, adding a new degree of freedom in precisely controlling the material properties.[1–4] Therefore, polymorphic materials offer unique properties for integrated electronics,[5] optoelectronics, and photonics.[6,7] In particular, the abrupt changes in the band structures in the material can be utilized to realize versatile transistors,[5,8,9] optical gratings, meta structures,[10] and photodetectors.[6,7] For example, the polymorphic materials are essential building blocks of current CMOS technology with seamless homojunction, facilitating wider depletion regions.[5]

The pursuit of polymorphic crystals at the nanoscale is both promising as well as challenging. Various strategies are utilized for this purpose, such as epitaxial growth,[5,11] chemical treatment,[9] block copolymer lithography coupled with etching,[12] and selective ion or electron beam patterning.[13] Most of these techniques suffer from non-uniform spatial control, multistep fabrication process, low throughput, and high instrumental cost. Compared to these, optical patterning is a spatially selective, and lithography-free process suitable for large-area samples, and requires only a conventional laser source and an objective lens.[14,15]

Here, we choose $MoTe_2$ as an example thanks to its rich polymorphic nature with the semiconducting 2H-phase and the metastable semi-metallic 1T′-phase.[9,16,17] As a result of the small electronegativity difference (≈0.3) between molybdenum (Mo) and tellurium (Te) atoms,[18] the phase transition between 2H and 1T′ phases occurs at relatively lower energy (<50 meV) compared to the other 2D semiconductor counterparts like MoS_2 and $MoSe_2$.[16,19] Due to the low phase transition barrier, polymorphism in $MoTe_2$ can be readily induced via optical modification.[16] In fact, laser-induced doping,[20,21] oxidation,[22] phase transition,[16,19] and etching[23] have been reported in $MoTe_2$. However, the optical characteristics of the engineered phases and their integration into the photonic and optoelectronic devices remain elusive.

In this work, we demonstrate a highly selective, lithography-free direct writing approach on multilayered $MoTe_2$ with a

F. Ahmed, H. A. Fernandez, Y. Zhang, A. M. Shafi, M. G. Uddin, X. Cui, H. H. Yoon, N. Mehmood, A. C. Liapis, Z. Sun, H. Lipsanen
Department of Electronics and Nanoengineering
Aalto University
P.O. Box 13500, FI-00076 Aalto, Finland
E-mail: faisal.ahmed@aalto.fi; harri.lipsanen@aalto.fi

C. Rodríguez-Fernández, H. Caglayan
Faculty of Engineering and Natural Science
Photonics
Tampere University
33720 Tampere, Finland

H. A. Fernandez, Y. Zhang, M. G. Uddin, X. Cui, H. H. Yoon, Z. Sun
QTF Center of Excellence
Department of Applied Physics
Aalto University
00076 Aalto, Finland

L. Yao
Department of Applied Physics
Aalto University
00076 Aalto, Finland

The ORCID identification number(s) for the author(s) of this article can be found under https://doi.org/10.1002/adfm.202302051.

DOI: 10.1002/adfm.202302051

continuous-wave visible laser to realize high-performance photonic and optoelectronic devices. To understand the dynamics of laser-induced optothermal effect, we performed systematic experiments and analysis with confocal Raman spectroscopy, micro-reflectance, atomic force microscopy, transmission electron microscopy, non-linear optics, electrical, and optoelectrical characterizations. After the phase change from semiconducting to metallic, the reflection contrast decreases from the near-infrared to telecom-band ranges (1–1.5 μm) mainly due to the change in the band structure and increase in surface roughness. As a result, the third harmonic generation (THG) intensity increases by seven times in 1T′-$MoTe_2$ compared to 2H-$MoTe_2$ with almost one order increase in conversion efficiency and susceptibility when pumped by the telecom-band laser. Lastly, we utilized these features to realize a polymorphic Schottky photodiode with a partially formed metallic phase in a semiconducting $MoTe_2$ channel.

2. Results and Discussion

Figure 1a shows the schematic of atomic structures of thermodynamically stable phases with the trigonal prismatic crystal structure of 2H-$MoTe_2$ (left panel) and the monoclinic 1T′ phase of $MoTe_2$ (right panel).[24,25] In the 2H-$MoTe_2$ phase, Mo atoms are sandwiched between two Te atoms in a hexagonally arranged fashion, while in 1T′-phase, Mo atoms form octahedral coordination around Te atoms in each layer, with lattice distortion around the *y*-axis. We started our experiment by cleaving multilayer (≈122 nm thick) 2H-$MoTe_2$ flakes from the bulk crystal on a standard Si substrate with 285 nm SiO_2 (see materials and method section and Figure S1 of Supplementary Information). The Raman scattering spectra observed in the 100 to 300 cm^{-1} range for the 2H-$MoTe_2$, measured with λ = 532 nm excitation and 500 μW, are shown in Figure 1b in black. All the measured multilayer 2H-$MoTe_2$ flakes exhibit two prominent peaks at 171 and 235 cm^{-1}, representing the out-of-plane (A_{1g}) and in-plane (E_{2g}) vibration modes respectively.[26] Subsequently, we obtain the critical value of the laser power required for the phase transition of the $MoTe_2$ flakes by gradually increasing the laser irradiation power, see Figure S2 of Supplementary Information. The optically induced phase change process is repeated for 20 different thickness (15–80 nm) flakes, and all the flakes exhibited transition around 8–10 mW power with λ = 532 nm laser. After irradiation, the dominant distorted octahedral structure of the 1T′-$MoTe_2$ phase can be identified by the appearance of new peaks located at 121 and 140 cm^{-1} related to the A_g mode (1T′ phase) and the dropping of Raman modes of 2H-phase as depicted in Figure 1b.[8,16]

The laser-induced thermal energy is responsible for inducing the irreversible phase transition from 2H to 1T′ by generating Te vacancies. With the increase of local flake temperature and Te vacancies, the phase transition temperature is decreased significantly, which accelerates the phase change process in $MoTe_2$.[16,17,19] Note that we realized polymorphism in $MoTe_2$ with a continuous wave green laser (532 nm) at <10 meV irradiation power in an ambient environment. Our mild optical conditions are appropriate for materials with low-phase transition energy such as $MoTe_2$. However, for materials with relatively large phase transition energy barrier, such as MoS_2 (≈400 meV),[27] polymorphism can be realized by choosing appropriate laser parameters such as laser power, wavelength, irradiation time, scanning speed, and employing transient (femtosecond) lasers.[14,28] Therefore, our approach can be extended to other polymorphic-rich 2D materials[29] like MoS_2, $MoSe_2$, In_2Se_3, TaS_2, and GaTe, etc., to deterministically realize polymorphism.

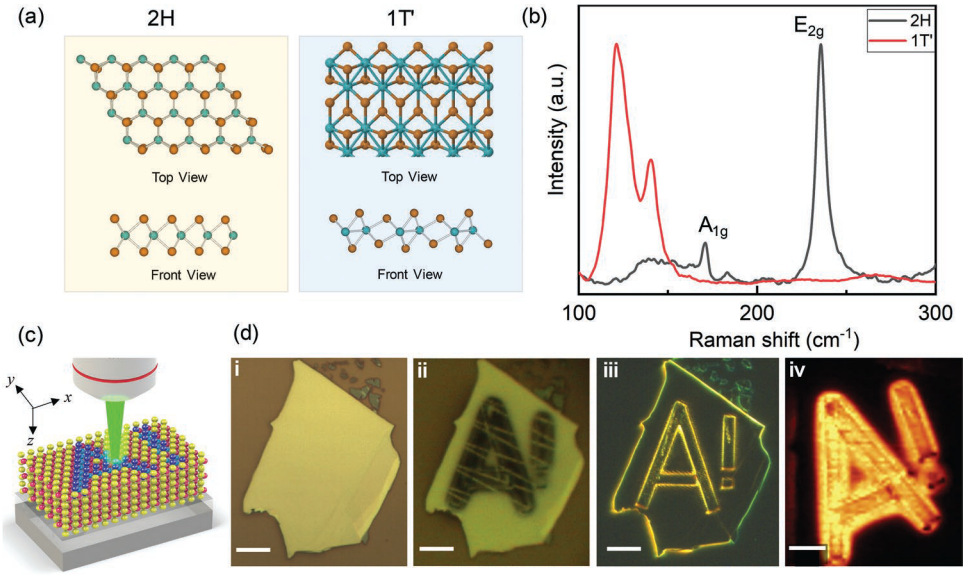

Figure 1. Polymorphic $MoTe_2$. a) The schematic of crystal structure of 2H (left panel) and 1T′ (right panel) $MoTe_2$. b) Raman spectra of 2H- and 1T′-$MoTe_2$ measured at 1 mW laser power. c) The schematic illustration of phase change with a focused 532 nm laser over $MoTe_2$ flake. d) i) Optical microscope image of as exfoliated multilayer 2H-$MoTe_2$ flake, ii) $MoTe_2$ flake after high power (9 mW) laser scanning in a given design, iii) The dark field optical image, and iv) Raman intensity map of 120 cm^{-1} mode of 1T′-$MoTe_2$ collected at 1 mW laser power. Scale bar is 5 μm.

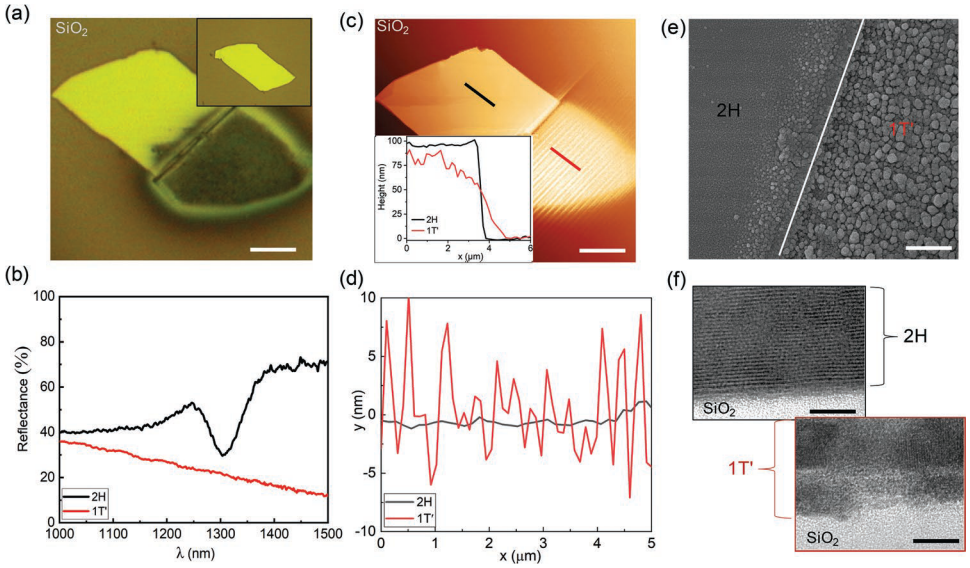

Figure 2. Optical and surface morphology analysis of polymorphic $MoTe_2$. a) The OM image of $MoTe_2$ after phase change with a laser probe. Inset is the OM image of as exfoliated flake. b) The reflectance spectrum 2H and 1T′-$MoTe_2$ from 1000 to 1500 nm range c) The topographic image of (a) collected by atomic force microscopy. Scale bar in (a) and (c) is 5 μm. d) the roughness profile along the dashed lines in (c). e) Scanning electron micrograph of polymorphic $MoTe_2$ with a white dashed demarcation line between 2H and 1T′-$MoTe_2$. Scale bar: 500 nm. f) Cross-section transmission electron microscope images of 2H (upper panel) and 1T′ (lower panel) $MoTe_2$. Scale bars: 5 nm.

After point measurements, we placed $MoTe_2$ sample over an x-y piezo-driven stage under high power (8 mW) laser, as depicted in Figure 1c to deterministically realize the polymorphic $MoTe_2$. The piezo-stage of Raman system enables the on-demand features with a resolution as small as ≈0.7 μm (1.2 λ/N.A. with 532 nm laser and 0.9 N.A.). As an example, we pattern the Aalto University logo (A!) on a 2H-$MoTe_2$ flake at 8 mW power, as shown in Figure 1d,i–iv representing optical microscope (OM) image in bright field, dark field, and Raman intensity map respectively. Interestingly, after phase change, the color contrast of $MoTe_2$ is changed, i.e., the laser-modified $MoTe_2$ portion becomes darker, see **Figure 2**a. To understand this, we performed the micro-reflectance analysis over a broad spectrum in the near-infrared to the telecom-band ranges. The collimated normal incidence beam is focused on the sample with an objective, and the collection of the signal was performed in the backscattering geometry, see materials and method section and Figure S3 of Supplementary Information. The reflectance is extracted as:

$$\text{Reflectance} = \frac{I_{\text{sample}} - I_{\text{dark}}}{I_{\text{ref}} - I_{\text{dark}}} \quad (1)$$

Where I_{sample} is reflected light intensity collected from $MoTe_2$ phases, I_{dark} is intensity without light, and I_{ref} is a 100 nm thick silver mirror. The reflectance spectra of a multilayer 2H-$MoTe_2$ and 1T′-$MoTe_2$, onto a Si substrate, are shown in Figure 2b. A spectral dip on the 2H-$MoTe_2$ phase is observed ≈1300 nm (0.95 eV), which is attributed to the well-known A intralayer exciton (e–h confined in the same layer) of bulk 2H-$MoTe_2$.[30,31] Interestingly, the 1T′-phase shows lower reflectance compared to the 2H-phase and the absence of excitonic transition across the measured spectrum. The 1T′-$MoTe_2$ is electrically metallic in nature, discussed in the later part of the manuscript. This is unlike traditional bulk metals, which are more reflective in the visible range. Due to the metallic nature of 1T′-$MoTe_2$, we did not observe the excitonic transition. These results suggest that the micro-reflectance analysis is a noninvasive and straightforward technique to distinguish the phase transition and change in band structure in nanoscale materials. Note that we have provided here micro reflectance measurements in the near-infrared region to observe the excitonic transition in multilayer 2H-$MoTe_2$. As indicated by the OM image, we observed a decrease in reflectance in 1T′-phase compared to 2H in the visible region, see Supplementary information, S4.

Additionally, the optical contrast in the layered 2D materials is thickness dependent,[32] and the thickness of the $MoTe_2$ flake is expected to decrease with the laser-induced optothermal effects.[23] To confirm this, we obtained the topography of polymorphic $MoTe_2$ with atomic force microscopy. The height profile in the inset of Figure 2c suggests that the thickness of 1T′-$MoTe_2$ decreases ≈13 ± 2 nm compared to 2H after laser irradiation. The laser-induced thermal effect enhances the temperature of the topmost layers to their sublimation point, thus reducing the thickness.[23] Meanwhile, the roughness (root mean square) of the flake increases from 1.82 to 6.55 nm as shown by the line profile in Figure 2d. The increase in roughness is also confirmed by high-resolution scanning electron micrograph in Figure 2e. The cross-sectional transmission electron microscope image depicts the intact layered structure of 2H-$MoTe_2$, see the upper panel in Figure 2f, whereas the layers are distorted in 1T′-$MoTe_2$ due to high energy optical patterning, see the lower panel in Figure 2f. More relevant results are provided in Figure S5–S7 of supplementary information. The laser-induced thinning and roughness enhancement can be precisely controlled by varying the incident power, and integration/exposure time.[23,33] This has been investigated elsewhere.[33] The increase in roughness

will scatter the incident normal light in arbitrary directions, thus the decrease in reflectance spectra for 1T′-phase is realized. In brief, the observed change in reflectance spectra is the combined effect of the laser-induced phase transition, corresponding band structure modulation, and changes in thickness and surface roughness.

Next, we investigate the non-linear optical effects in both phases of polymorphic $MoTe_2$. Although there are some studies with a focus on the second-order optical nonlinearities in 2H- and 1T′-$MoTe_2$ to investigate the crystal symmetry.[8,34,35] The third-order nonlinear effect, such as third harmonic generation (THG) in polymorphic $MoTe_2$ has not been fully revealed.[36] Unlike the strict requirement of materials' symmetry breaking in second harmonic generation (SHG), THG occurs in all materials in principle and has been successfully demonstrated in applications, such as label-free live brain imaging,[37] high-efficiency frequency up-conversion in the nanoparticles and plasmonic antenna hybrid system,[38] characterizing the fine structural distortion of atomically thin materials,[39] and ultrafast chiral all-optical switch.[40] For this, we exfoliated multilayer 2H-$MoTe_2$ flake and optically modified the half portion of 2H flake to 1T′, see OM image and Raman intensity of 120 cm^{-1} in **Figure 3**a,b respectively. The femtosecond laser with λ = 1500 nm (≈2 μW, corresponding to 28.84 GW cm^{-2}) is employed to obtain THG, see the method section for more experimental details. Figure 3c shows that 1T′-$MoTe_2$ exhibits seven times stronger THG intensity than 2H-$MoTe_2$. Figure 3d shows the peak intensity of the THG signal along the dashed red curve shown in Figure 3a, which shows consistent results that 1T′-$MoTe_2$ has a stronger THG signal compared to the 2H-$MoTe_2$. The measured THG conversion efficiency of 1T′- and 2H-$MoTe_2$ are ≈1.7×10^{-7} and ≈1.7×10^{-8}, respectively. Furthermore, the calculated effective third-order susceptibilities are 1.1×10^{-19} and 0.3×10^{-19} m^2 V^{-2} for 1T′-and 2H-phase, respectively. THG enhancement in 1T′-$MoTe_2$ might be due to its higher absorption at the pump wavelength of 1500 nm as given in Figure 2b. Additionally, the laser-induced tellurium vacancy generation might have contributed to enhancing the THG intensity of 1T′-$MoTe_2$.[41] Our results can provide a simple route for defect visualization by employing THG microscopy. Considering the thickness of the $MoTe_2$ used in the THG measurements, it is reasonable that the measured nonlinear conversion efficiency is higher than monolayer transition metal dichalcogenides (e.g., MoS_2).[42,43] This can be beneficial to use the laser-induced 1T′-$MoTe_2$ for various non-linear optical applications such as optical harmonic generation, saturable absorbers, ultrafast mode lock lasers, and broadband light conversion. Note that we did not observe second harmonic generation in either phase of multilayer $MoTe_2$ crystals within the detection limits of our setup. This observation agrees with the literature.[35,36]

Inspired by the improvements in the optical properties discussed so far, we focused on electrical and optoelectrical devices. We prepared a back-gated multilayer-$MoTe_2$-based field-effect-transistor before (**Figure 4**a,b) and after (Figure 4c,d) the phase transition from 2H to 1T′ with a high-power laser probe. Subsequently, we measured the typical output (I_{SD}-V_{DS}, where I_{SD} and V_{SD} are the source-to-drain current and voltage respectively) and transfer curves (I_{SD}-V_{GS}, where V_{GS} is the gate

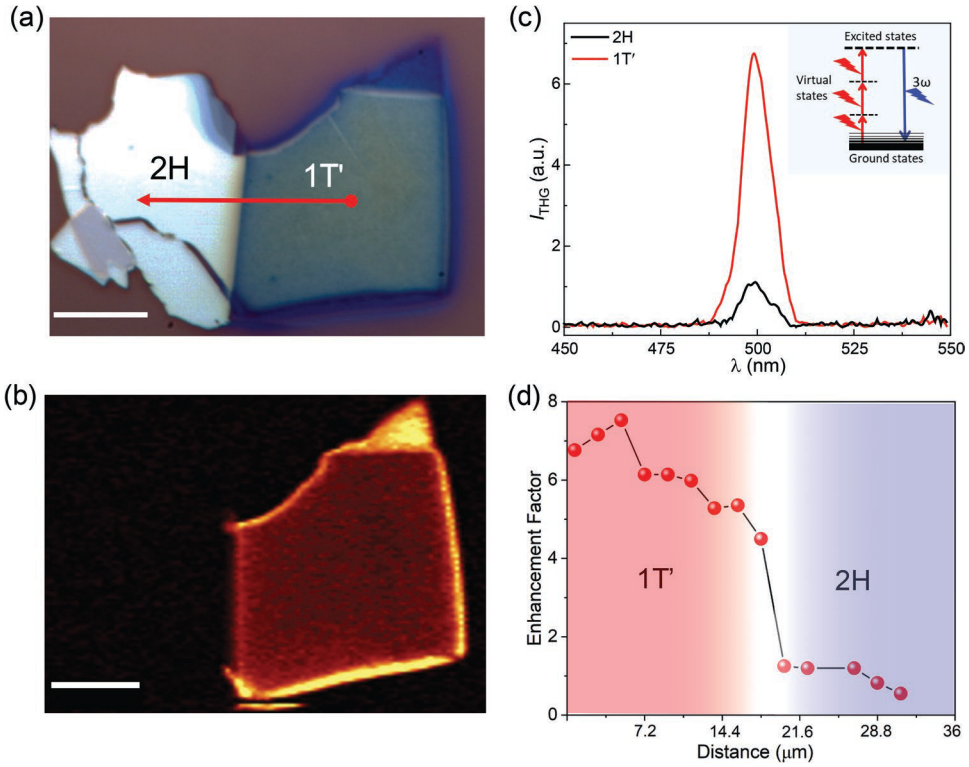

Figure 3. Nonlinear optical response of polymorphic $MoTe_2$. a) The OM image of polymorphic $MoTe_2$ with half phase change with a laser probe. b) The Raman intensity map of 1T′ Raman mode at 120 cm^{-1} with a spectra width of 15 cm^{-1}. Scale bar in (a) and (b) is 10 μm. c) the third harmonic generation intensity of polymorphic $MoTe_2$. d) the line scan of THG along the red line.

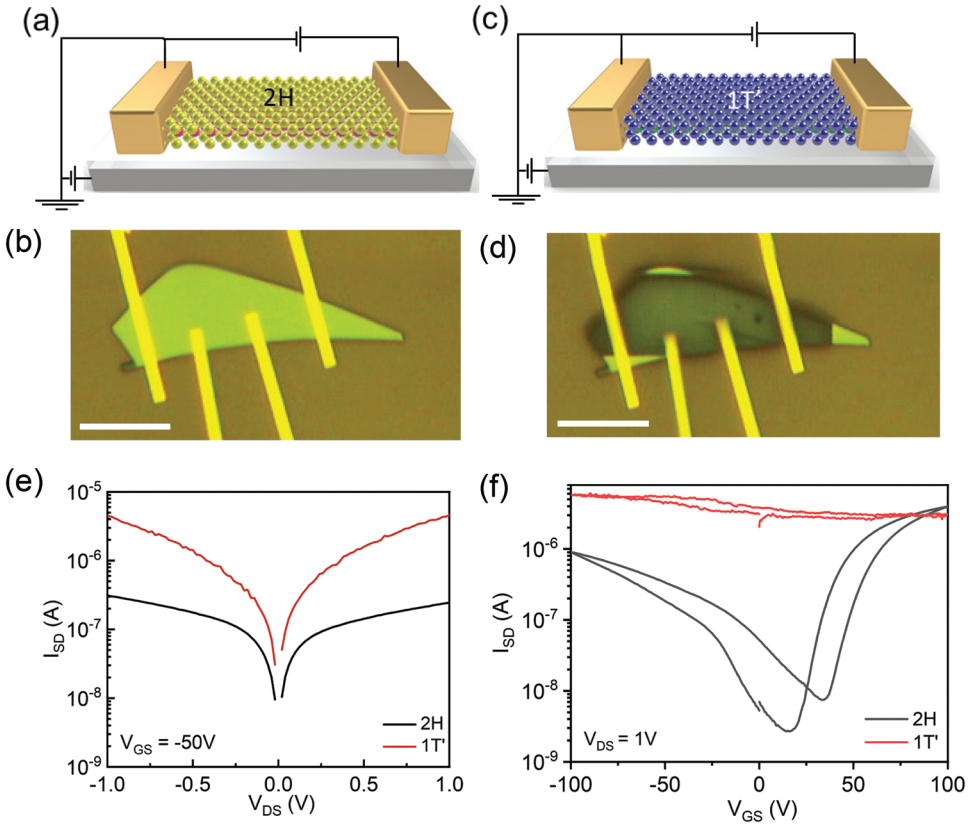

Figure 4. Electrical characteristics of polymorphic $MoTe_2$. (a) and (b) the schematic diagram and OM image of 2H and 1T′-$MoTe_2$ respectively. (c) and (d) the OM image of 2H and 1T′-$MoTe_2$ after laser irradiation respectively. (e) and (f) the respective output and transfer curves of 2H and 1T′-$MoTe_2$ at given bias conditions.

voltage applied across source-to-gate electrodes) for both cases under the same biasing conditions. The I_{SD}-V_{DS} plots for both phases show quasi-linear behavior at V_{GS} = −50 V, indicating low resistive contacts between the contact electrode (Ti) and the channel. However, the I_{SD} level for the 1T′ phase is higher than that of the 2H phase, confirming a less resistive metallic 1T′ phase. The double sweep I_{SD}-V_{GS} plot for the 2H-phase exhibits ambipolar behavior with the on/off ratio of ≈10^4 (10^3) for the electron (hole) branch. The slight dominant electron branch suggests that the Fermi level is aligned slightly closer to the conduction band edge compared to the valence band edge.[44] After phase transition, the metallic phase shows an increased current level, hence increased electrical conductivity, and decreased on/off ratio. Interestingly, the transfer curve of 1T′ phase transistor is almost flat because of immunity to gate modulation in a highly conductive metallic channel. It is expected that the $MoTe_2$ channel beneath the electrode might remain intact, nonetheless, the device operation characteristics in a highly conductive channel are likely to be dominant by the channel rather than contacts. These results suggest that the $MoTe_2$ channel remains electrically active after high-power laser irradiation.

As mentioned earlier, polymorphic materials are an indispensable part of all the electronics and optoelectronics devices such as flash memories, programmable logic gates, memories, photodetectors, light-emitting diodes, etc. The metal-semiconductor diodes are advantageous over p-njunction diodes due to their selective doping-free fabrication, low power consumption, and low dark current in optoelectronic device applications. Therefore, utilizing the polymorphic properties of $MoTe_2$, we partially induced the metallic phase in a semiconducting $MoTe_2$ channel to form a metal-semiconductor junction, i.e., a Schottky diode, as shown in **Figure 5**a inset. We firstly evaluated the polymorphic $MoTe_2$-based Schottky diode characteristics under dark, and for this, we collected output curves, as shown in Figure 5a. Our device shows a forward rectifying behavior such that the forward-bias current is much higher than the reverse-bias current for all measured V_{GS} values. The rectification ratio (ratio of forward bias current to the reverse bias current) is ≈20, which is comparable to the reported 2D materials-based diodes.[45] The ideality factor (η) is used to benchmark the diode performance with respect to an ideal diode. It is quantitatively computed by fitting the diode characteristics with the diode model, as:

$$I = I_s\left[\exp\left(\frac{qV_{DS}}{\eta K_B T} - 1\right)\right] \quad (2)$$

where I is the diode current, I_S is the reverse bias saturation current, q is elementary charge, K_B is Boltzmann constant, and T is temperature. Our 2H/1T′ $MoTe_2$ Schottky diode shows η ≈2.8, and this value can be further improved by optimizing

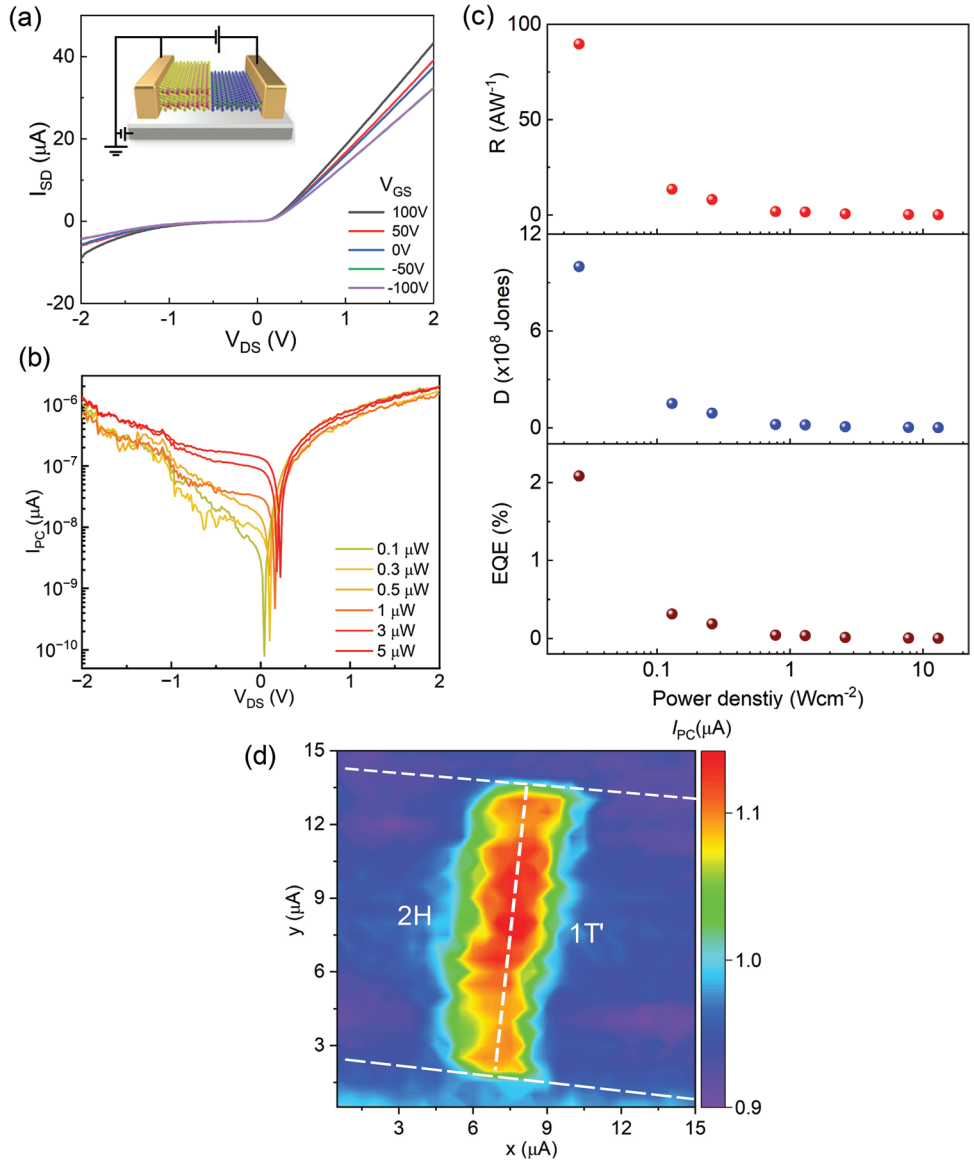

Figure 5. Optoelectrical characteristics of polymorphic $MoTe_2$ junction. a) The output curves of 2H- and 1T′-$MoTe_2$ based Schottky diode in dark conditions. Inset: Schematic diagram of the polymorphic diode. b) The device photocurrent at different laser powers. c) Optical responsivity, detectivity, and external quantum efficiency as a function of illumination power density, and d) the photocurrent mapping plot measured near the 2H/1T′ interface with 532 nm laser at $V_{DS} = -1$ V.

channel thickness.[45] Our device exhibits weak gate modulation, also see Figure S8 of supplementary information, perhaps due to the dominant contribution from the metallic 1T′-phase in the overall conductivity of the polymorphic $MoTe_2$ channel.

We investigated the photodetection characteristics of our polymorphic Schottky diode by illuminating a 532 nm focused laser. Figure 5c inset summarizes the photocurrent ($I_P = I_{light}$-I_{dark}, where I_{light} is I_{SD} under light illumination and I_{dark} is the I_{SD} in dark) at different incident light power values. Interestingly, with the increase of laser power, the photocurrent minima shift toward positive V_{DS}, alternatively, the increase in zero bias current is realized. These trends suggest that our Schottky diode functions as a photovoltaic cell with sufficient open circuit voltage and short circuit current under given illumination conditions.[45,46]

We used these data sets to calculate the figure-of-merits of a photodetector, such as photoresponsivity ($R = I_P/P$, where P is the laser power), and photo-detectivity ($D^* = R\sqrt{\frac{A}{2qI_{dark}}}$, where A is the effective illumination area). The obtained R and D^* values are plotted as a function of power density in Figure 5c. Our 2H/1T′ $MoTe_2$ junction device shows $R \approx 90$ AW^{-1} and $D^* \approx 10^9$ Jones at 0.1 W cm^2 power density. Similarly, external quantum efficiency ($EQE = R\frac{hc}{q\lambda}$, where h is Planck's constant and c is speed of light) is the measure of the optical gain of a photodetector. Our polymorphic $MoTe_2$ device shows a maximum EQE of ≈2%. The obtained R, D^*, and EQE values decrease with the increase of illumination power due to the saturation of photoex-

cited charge carrier generation at higher power densities. These obtained values are significantly higher than the reported values for only $MoTe_2$-based photodetectors.[47]

We used the scanning photocurrent microscopy technique to investigate the spatial location of photoexcited charge carriers in our polymorphic device. For this, we selected an active channel area of ≈15 × 15 μm^2 covering 2H and 1T′ phases and collected the I_{SD} while scanning the focused laser (532 nm laser, 10 μW power) at V_{GS} = 50 V and V_{DS} = −1 V. The obtained 2D spatial map of the photoresponse of the device in Figure 5d suggests that the photoexcited charge carriers are concentrated along the 2H/1T′ junction in the polymorphic $MoTe_2$ channel. Typically, a Schottky barrier is formed when a metallic material comes in contact with a semiconductor. The Schottky barrier induces the internal electrical field that separates the photoexcited charge carriers in an optically active device. Similarly, the effective carrier separation of photoexcited charge carriers across the built-in potential induced by the 2H/1T′ $MoTe_2$ Schottky interface leads to the enhanced photodetection performance in our polymorphic $MoTe_2$.[46] Besides revealing the spatial location of photocarriers, these results also explain the mechanism of photogeneration in the polymorphic $MoTe_2$ device. In brief, our results suggest the superiority of using polymorphic channels compared to only semiconducting channels for optoelectronic applications. This concept can be further extended by designing alternative metal-semiconductor strips at micron or nanoscale such as optical gratings to investigate interesting light-matter interactions in the future.

3. Conclusion

In conclusion, we have directly modulated the polymorphic characteristics of $MoTe_2$ on the micron scale by using a visible laser probe for photonic, and optoelectronic applications. The laser-induced metallic phase $MoTe_2$ has different optical contrast in near-infrared to telecom-band ranges (1–1.5 μm) compared to semiconducting $MoTe_2$ due to the abrupt changes in its band structure and increase in surface roughness. This leads to around seven times enhancement in third harmonic generation upon telecom band excitation with enhanced effective conversion efficiency and third-order non-linearity. Lastly, we have realized a Schottky diode with enhanced photoresponse based on polymorphic engineering by intentionally forming half of the semiconducting $MoTe_2$ as metallic $MoTe_2$. We believe the polymorphic engineered structures will greatly benefit the 2D-materials-based integrated photonics circuits and optoelectronic applications.

4. Experimental Section

Sample and Device Preparation: The multilayer $MoTe_2$ flakes were exfoliated from the bulk $MoTe_2$ crystal (2D Semiconductors) using the standard scotch-tape technique on a solvent cleaned *p*-doped silicon substrate (0.001–0.005 Ω cm) with thermally grown 285 nm thick SiO_2. The candidate flakes were used for laser patterning. For field-effect-transistor fabrication, electron beam lithography (EBL Vistec, EPBG 5000), and metallization (5 nm Ti, and 50 nm Au) were carried out by electron beam evaporator (MASA, IM-9912) under ≈10^{-7} torr pressure followed by lift-off to remove excessive metals. The height and roughness of the targeted flakes were determined using an atomic force microscope (Bruker, Dimension Icon).

Raman Measurements: Raman spectroscopy measurements were performed with a micro-Raman system (WITec alpha300 RA+) in a confocal backscattering geometry. A frequency-doubled Nd:YAG solid-state laser of 532 nm wavelength was used as excitation. The linearly polarized excitation light was focused perpendicularly (along the z-direction) onto the samples using 100 × objective (NA = 0.95) with a spot size of ≈1 μm^2. The backscattered photons were collected via the same microscope objective and subsequently analyzed in a spectrometer equipped with a grating of 1800 mm^{-1} gratings to obtain Raman spectra that were detected by a Si-charge-coupled camera. All experiments were performed at room temperature.

Reflectance Measurements: The samples were characterized using a WITec alpha300C confocal microscope. The samples were illuminated with a broadband light source (LDLS EQ-99X) through a Zeiss EC "Epiplan" DIC, 20× objective (NA = 0.4, WD = 3.0 mm). The spectral response was collected through the same objective and coupled to an ultra-high throughput spectrometer (UHTS300) for the visible spectrum and NIR-Quest (Ocean optics NIR Flame) detector for the IR region using an optical fiber. Also, see Supplementary Information S3.

Nonlinear Optical Measurements: The fundamental wave with a center wavelength of ≈1500 nm for THG comes from an amplified Ti:sapphire femtosecond laser system (Spectra-Physics, Solstice Ace) with a repetition rate of ≈2 kHz and pulse duration ≈130 fs. The beam is focused onto the sample with an objective lens (NA = 0.75, 40×, Nikon) with a beam spot diameter of ≈2 μm. The reflected THG signal was collected by the same objective lens and directed to a spectrograph (Andor) supplied with a photomultiplier tube (Hamamatsu), and the recorded data is sampled by a lock-in amplifier (Stanford research system). Note that two short pass filters (Edmund) were used to block the fundamental wave before the reflected light from the sample enters the spectrograph.

Electrical and Optoelectrical Measurements: The fabricated device chips were mounted on a printed circuit board with wire bonding. All the electrical measurements were carried out with an optical microscope (WITec Alpha 300 RA+) coupled with two source meters (Keithley 2400 and 2401) at room temperature under ambient conditions. The gate voltage was applied to the Si substrate, while the source and drain voltages were applied to the metal electrodes connected to the $MoTe_2$ channel. The photocurrent measurements were conducted in the WITec system coupled with two source meters. The light beams from continuous-wave lasers at 532 nm (WITec focus innovations) were focused onto the heterojunction through an objective lens (Nikon CF Plan 100×, NA = 0.95). The optical microscopy platform system allowed us to focus the laser beam on desired positions in the sample.

Supporting Information

Supporting Information is available from the Wiley Online Library or from the author.

Acknowledgements

This research was supported by the Academy of Finland [Grant No. 320167 (PREIN Flagship – Aalto University)], Grant No. 320165 (PREIN Flagship – Tampere University)], and GrapheneCore3 number 881603. Academy of Finland (314810, 333982, 336144, 336818, and 348920), the European Union's Horizon 2020 research and innovation program (820423,S2QUIP, Marie Sklodowska-Curie grant agreement N° 895369), the EU H2020-MSCA-RISE-872049 (IPN-Bio), ERC (834742), and Horizon Europe (HORIZON) Project: ChirLog (101067269). The authors would like to acknowledge the provision of facilities and technical support from the Otaniemi research infrastructure (OtaNano-Micronova Nanofabrication Centre and OtaNano-Nanomicroscopy Centre).

Conflict of Interest

The authors declare no conflict of interest.

Data Availability Statement

The data that support the findings of this study are available from the corresponding author upon reasonable request.

Keywords

molybdenum ditelluride, phase change, polymorphic, reflectance, Schottky photodiode, third harmonic generation

Received: February 21, 2023
Revised: March 28, 2023
Published online: April 28, 2023

[1] H. Bergeron, D. Lebedev, M. C. Hersam, *Chem. Rev.* **2021**, *121*, 2713.
[2] W. Li, X. Qian, J. Li, *Nat. Rev. Mater.* **2021**, *6*, 829.
[3] D. Voiry, A. Mohite, M. Chhowalla, *Chem. Soc. Rev.* **2015**, *44*, 2702.
[4] X. Wang, Z. Song, W. Wen, H. Liu, J. Wu, C. Dang, M. Hossain, M. A. Iqbal, L. Xie, *Adv. Mater.* **2019**, *31*, 1804682.
[5] J. H. Sung, H. Heo, S. Si, Y. H. Kim, H. R. Noh, K. Song, J. Kim, C.-S. Lee, S.-Y. Seo, D.-H. Kim, H. K. Kim, H. W. Yeom, T.-H. Kim, S.-Y. Choi, J. S. Kim, M.-H. Jo, *Nat. Nanotechnol.* **2017**, *12*, 1064.
[6] Q. Wang, E. T. F. Rogers, B. Gholipour, C. M. Wang, G. Yuan, J. Teng, N. I. Zheludev, *Nat. Photonics* **2016**, *10*, 60.
[7] M. Wuttig, H. Bhaskaran, T. Taubner, *Nat. Photonics* **2017**, *11*, 465.
[8] Y. Wang, J. Xiao, H. Zhu, Y. Li, Y. Alsaid, K. Y. Fong, Y. Zhou, S. Wang, W. Shi, Y. Wang, A. Zettl, E. J. Reed, X. Zhang, *Nature* **2017**, *550*, 487.
[9] R. Kappera, D. Voiry, S. E. Yalcin, B. Branch, G. Gupta, A. D. Mohite, M. Chhowalla, *Nat. Mater.* **2014**, *13*, 1128.
[10] J. Kim, C. Park, J. W. Hahn, *Adv. Opt. Mater.* **2022**, *10*, 2101930.
[11] K.-A. N. Duerloo, Y. Li, E. J. Reed, *Nat. Commun.* **2014**, *5*, 4214.
[12] T. Yun, H. M. Jin, D. Kim, K. H. Han, G. G. Yang, G. Y. Lee, G. S. Lee, J. Y. Choi, I. Kim, S. O. Kim, *Adv. Funct. Mater.* **2018**, *28*, 1804508.
[13] Y. C. Lin, D. O. Dumcenco, Y. S. Huang, K. Suenaga, *Nat. Nanotechnol.* **2014**, *9*, 391.
[14] S. M. Akkanen, H. A. Fernandez, Z. Sun, *Adv. Mater.* **2022**, *34*, 2110152.
[15] M. Wang, D. Li, K. Liu, Q. Guo, S. Wang, X. Li, *ACS Nano* **2020**, *14*, 11169.
[16] S. Cho, S. Kim, J. H. Kim, J. Zhao, J. Seok, D. H. Keum, J. Baik, D.-H. Choe, K. J. Chang, K. Suenaga, S. W. Kim, Y. H. Lee, H. Yang, *Science.* **2015**, *349*, 625.
[17] D. H. Keum, S. Cho, J. H. Kim, D.-H. Choe, H.-J. Sung, M. Kan, H. Kang, J.-Y. Hwang, S. W. Kim, H. Yang, K. J. Chang, Y. H. Lee, *Nat. Phys.* **2015**, *11*, 482.
[18] J. Bernède, C. Amory, L. Assmann, M. Spiesser, *Appl. Surf. Sci.* **2003**, *219*, 238.
[19] Y. Tan, F. Luo, M. Zhu, X. Xu, Y. Ye, B. Li, G. Wang, W. Luo, X. Zheng, N. Wu, Y. Yu, S. Qin, X. A. Zhang, *Nanoscale* **2018**, *10*, 19964.
[20] S. Y. Seo, J. Park, J. Park, K. Song, S. Cha, S. Sim, S. Y. Choi, H. W. Yeom, H. Choi, M. H. Jo, *Nat. Electron.* **2018**, *1*, 512.
[21] S.-Y. Seo, G. Moon, O. F. N. Okello, M. Y. Park, C. Han, S. Cha, H. Choi, H. W. Yeom, S.-Y. Choi, J. Park, M.-H. Jo, *Nat. Electron.* **2021**, *4*, 38.
[22] S. Mukherjee, D. Dutta, P. K. Mohapatra, L. Dezanashvili, A. Ismach, E. Koren, *ACS Nano* **2020**, *14*, 17543.
[23] A. Castellanos-Gomez, M. Barkelid, A. M. Goossens, V. E. Calado, H. S. J. Van Der Zant, G. A. Steele, *Nano Lett.* **2012**, *12*, 3187.
[24] N. Mounet, M. Gibertini, P. Schwaller, D. Campi, A. Merkys, A. Marrazzo, T. Sohier, I. E. Castelli, A. Cepellotti, G. Pizzi, N. Marzari, *Nat. Nanotechnol.* **2018**, *13*, 246.
[25] N. M. Nicolas Mounet, M. Gibertini, P. Schwaller, D. Campi, A. Merkys, A. Marrazzo, T. Sohier, I. E. Castelli, A. Cepellotti, G. Pizzi, *Mater. Cloud Arch.* **2020**, 158.
[26] F. Ahmed, A. M. Shafi, D. M. A. Mackenzie, M. A. Qureshi, H. A. Fernandez, H. H. Yoon, M. G. Uddin, M. Kuittinen, Z. Sun, H. Lipsanen, *Adv. Mater. Interfaces* **2021**, *8*, 2100950.
[27] Y. Guo, D. Sun, B. Ouyang, A. Raja, J. Song, T. F. Heinz, L. E. Brus, *Nano Lett.* **2015**, *15*, 5081.
[28] H. Yang, S. W. Kim, M. Chhowalla, Y. H. Lee, *Nat. Phys.* **2017**, *13*, 931.
[29] Z. Qian, L. Jiao, L. Xie, *Chinese J. Chem* **2020**, *38*, 753.
[30] A. Arora, M. Drüppel, R. Schmidt, T. Deilmann, R. Schneider, M. R. Molas, P. Marauhn, S. Michaelis De Vasconcellos, M. Potemski, M. Rohlfing, R. Bratschitsch, *Nat. Commun.* **2017**, *8*, 1703.
[31] G. Froehlicher, E. Lorchat, S. Berciaud, *Phys. Rev. B* **2016**, *94*, 085429.
[32] Y. Niu, S. Gonzalez-Abad, R. Frisenda, P. Marauhn, M. Drüppel, P. Gant, R. Schmidt, N. S. Taghavi, D. Barcons, A. J. Molina-Mendoza, S. M. de Vasconcellos, R. Bratschitsch, D. P. De Lara, M. Rohlfing, A. Castellanos-Gomez, *Nanomaterials* **2018**, *8*, 725.
[33] M. T. Turunen, E. Hulkko, K. K. Mentel, X. Bai, S. Akkanen, M. Amini, S. Li, H. Lipsanen, M. Pettersson, Z. Sun, *Adv. Mater. Interfaces* **2021**, *8*, 2002119.
[34] R. Beams, L. G. Cançado, S. Krylyuk, I. Kalish, B. Kalanyan, A. K. Singh, K. Choudhary, A. Bruma, P. M. Vora, F. Tavazza, A. V. Davydov, S. J. Stranick, *ACS Nano* **2016**, *10*, 9626.
[35] Y. Song, R. Tian, J. Yang, R. Yin, J. Zhao, X. Gan, *Adv. Opt. Mater.* **2018**, *6*, 1701334.
[36] S. Ha, H. Kim, H. Nam, J. Choi, K. Chae, J.-U. Lee, J.-Y. Park, Y. Yoo, D.-I. Yeom, *ACS Photonics* **2022**, *9*, 2600.
[37] S. Witte, A. Negrean, J. C. Lodder, C. P. J. de Kock, G. Testa Silva, H. D. Mansvelder, M. Louise Groot, *Proc Natl Acad Sci USA* **2011**, *108*, 5970.
[38] H. Aouani, M. Rahmani, M. Navarro-Cía, S. A. Maier, *Nat. Nanotechnol.* **2014**, *9*, 290.
[39] J. Liang, T. Tu, G. Chen, Y. Sun, R. Qiao, H. Ma, W. Yu, X. Zhou, C. Ma, P. Gao, H. Peng, K. Liu, D. Yu, *Adv. Mater.* **2020**, *32*, 2002831.
[40] Y. Zhang, X. Bai, J. Arias Muñoz, Y. Dai, S. Das, Y. Wang, Z. Sun, *Light Sci Appl* **2022**, *11*, 216.
[41] L. Karvonen, A. Säynätjoki, M. J. Huttunen, A. Autere, B. Amirsolaimani, S. Li, R. A. Norwood, N. Peyghambarian, H. Lipsanen, G. Eda, K. Kieu, Z. Sun, *Nat. Commun.* **2017**, *8*, 15714.
[42] A. Autere, H. Jussila, Y. Dai, Y. Wang, H. Lipsanen, Z. Sun, *Adv. Mater.* **2018**, *30*, 1705963.
[43] A. Autere, H. Jussila, A. Marini, J. R. M. Saavedra, Y. Dai, A. Säynätjoki, L. Karvonen, H. Yang, B. Amirsolaimani, R. A. Norwood, N. Peyghambarian, H. Lipsanen, K. Kieu, F. J. G. de Abajo, Z. Sun, *Phys. Rev. B* **2018**, *98*, 115426.
[44] F. Ahmed, M. S. Choi, X. Liu, W. J. Yoo, *Nanoscale* **2015**, *7*, 9222.
[45] M. F. Khan, F. Ahmed, S. Rehman, I. Akhtar, M. A. Rehman, P. A. Shinde, K. Khan, D. Kim, J. Eom, H. Lipsanen, Z. Sun, *Nanoscale* **2020**, *12*, 21280.
[46] H. H. Yoon, F. Ahmed, Y. Dai, H. A. Fernandez, X. Cui, X. Bai, D. Li, M. Du, H. Lipsanen, Z. Sun, *ACS Appl. Mater. Interfaces* **2021**, *13*, 58927.
[47] T. J. Octon, V. K. Nagareddy, S. Russo, M. F. Craciun, C. D. Wright, *Adv. Opt. Mater.* **2016**, *4*, 1750.